

# Identifying Changes to Environmental Temporal Autocorrelation under Climate Change

Benedikt Farag

Department of Statistics and Data Science

Yale University

December 13, 2025

**Advised By:** Brian Macdonald, Department of Statistics and Data Science  
Wyatt Petryshen, Department of Earth & Planetary Sciences

## Abstract

Although the primary focus of the effects of anthropogenic climate change are in changes to average conditions, alterations in the overall distribution of climate are also to be expected. An example of such changes are alterations to temporal autocorrelation, which has a significant impact on the ecosystem stability and extinction risk by influencing the duration of extreme temperatures. Several previous studies have studied climate model simulations to quantify these trends over time. This study uses reanalysis data from the ERA5 database from 2000 to 2020 to investigate changes in surface air temperature across the United States. We introduce *Lowess-processing* of Power Spectrum Density (PSD) spectrum to isolate the stochastic response from periodic (harmonic) fluctuations present in the data. To quantify the temporal autocorrelation, we used a piecewise Generalized Least Squares model with Auto-Regressive errors (GLSAR), which provides a superior fit to the PSD compared to single slope estimates. Our results show a redistribution of temperature variability across timescales, with long timescale temporal autocorrelation ( $> 24$  hours) decreasing for major regions of the continental US, including the Pacific Northwest, Midwest, South Eastern US, and New England. Conversely, short timescale temporal autocorrelation ( $< 24$  hours) increased across most of the continental US, indicating enhanced daily-scale temperature persistence that may contribute to extended duration of heat waves and cold spells. The temporal autocorrelation was compared to the GLAD

land cover dataset, which revealed a negative relationship between urbanization and low frequency spectral exponents over time. These findings suggest that climate change is influencing the persistence and autocorrelation of temperature. Our code is available at <https://github.com/benedikt20/temporal-autocorrelation>.

## Introduction

This project aims to determine whether a discernible change in temporal autocorrelation of air temperature, over the first part of the 21st century, has occurred under anthropogenic climate change. Temporal autocorrelation quantifies how a variable is correlated to its past values, revealing patterns like trends and seasonality. In terms of climate variables, it quantifies how environmental conditions are related to the past, that describes the persistence of environmental fluctuations in time. Understanding temporal autocorrelation of such variables is important as it can influence extinction risk and ecosystem stability [9]. Recent works in this area have analyzed climate data taken from climate model simulations (CMIP5) spanning 1871 to 2099, as e.g. [2]. However, these results have not been validated against observationally constrained model data that more accurately represent past and current temporal autocorrelation. These results also lack additional exploration in its relationships with land cover change, which may play a significant role in mitigating or exaggerate, such impacts. Here, the ERA5 reanalysis data set will be used to estimate temporal autocorrelation. This data set is well suited for the analysis, providing observational interpolated data, which was selected to be the most accurate for US temperatures by NOAA. The data will be obtained from the [ERA5 database](#) as NetCDF files, with time, latitude and longitude coordinates. The latitude and longitude resolution is  $0.25^\circ$  and the time resolution is at 1 hour measurements ranging from 1940 to date. To limit the size of the data, a sub-region of the world will be selected for this project, covering the United States.

Here we will focus on determining the best methodology for estimating temporal autocorrelation. A common method in the literature (e.g., [2, 4]) is to quantify temporal autocorrelation as the spectral exponent  $\beta$  as the (negative) OLS estimated slope of the power spectrum in log-log space, based on the power-law relationship:

$$P(f) \propto \alpha f^{-\beta} \quad \text{i.e.} \quad P(f) \propto \frac{\alpha}{f^\beta} \quad (1)$$

However, the observed relationship does often not follow a clear linear trend which can deviate the results. Therefore, we will explore other approaches along with piecewise regression with use of breakpoint analysis. Since temperature time-series include stochastic and periodic components (e.g. daily cycles), the stochastic response must be isolated for our analysis herein. Periodic variability typically exhibits much higher power than

stochastic variability, which has the potential to significantly bias estimations of temporal autocorrelation.

The estimated temporal autocorrelation will then be compared to land cover change based on the [GLAD](#) dataset which quantifies changes in forest extent, cropland and urban regions etc. [7]. The dataset provides land cover classification for every five years from 2000-2020, which will be utilized to investigate the relationship between temporal autocorrelation and land cover change. The dataset has a 30-m spatial resolution, which is much more fine-grained than the ERA5 datasets and will be up-sampled to match the ERA5 grid of  $0.25^\circ$ .

## Data Exploration and Visualization

### Temperature Time Series

The data was downloaded from the ERA5 database for the boundary box in Table 1 on hourly intervals for five discrete years (2000, 2005, ..., 2020). Each time period is an equally gridded area of size  $0.25^\circ$ , resulting in a 24,341 data points per timestep. Figure 1 shows the raw data on January 1st 2020 along with state boundaries of the US.

Table 1: Spatial boundary box

Coordinate	Min	Max
Latitude	$25.0^\circ\text{N}$	$50.0^\circ\text{N}$
Longitude	$130.0^\circ\text{W}$	$70.0^\circ\text{W}$

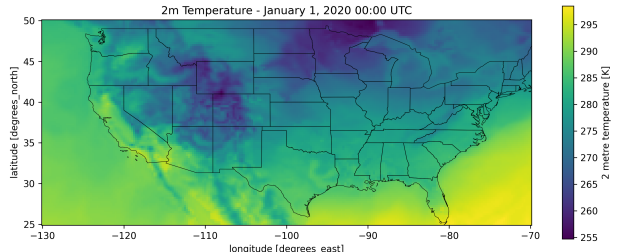


Figure 1: Raw data on January 1st 2020

The data was transformed to the frequency domain using the Multitaper Method (MTM) [3] with bandwidth  $NW = 2$  and tapers  $K = 3$ , that are commonly used parameters to minimize spectral leakage for a fixed time interval (one year in our case). Figure 2 shows the power-spectral density (PSD) along with the raw time-series for an example coordinate  $\mathcal{S}$ :

$$\mathcal{S} = (\text{lat} = 40^\circ\text{N}, \text{lon} = 100^\circ\text{W}, \text{year} = 2020)$$

The presence of the harmonic frequencies clearly appear as the localized spectral peaks. These peaks correspond primarily to the daily cycle ( $\log_{10} f^{day} = -1.38$ ) and its higher-order harmonics (e.g., 12 and 8 hour cycles), which arise due to asymmetric diurnal heating and cooling mechanisms. This causes the harmonic signal to be distributed among integer

multiples of the daily cycles in the frequency domain. These harmonics must be removed in order to isolate the stochastic component to estimate the spectral component  $\beta$  of the PSD spectrum [4].

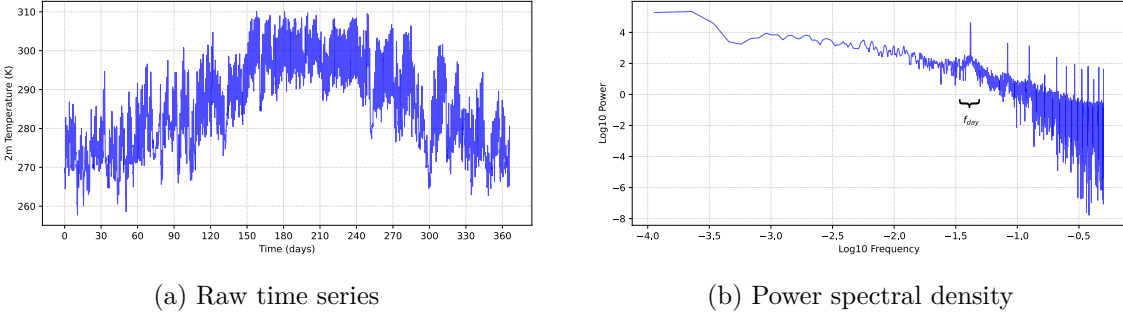


Figure 2: Raw data and PSD for the location  $\mathcal{S}$

While MTM analysis tries to minimize spectral leakage [3], the finite time interval inherently causes spectral leakage of power into adjacent bins [6]. This is caused by a convolution of a finite-time window function which causes a true harmonic frequency behavior to “leak” into nearby frequencies. This behavior arises in Figure 2, especially around the daily frequency, where nearby powers appear as a local bump in the power-frequency relationship.

There are several existing models that are commonly used to describe the stochastic background of time-series. The simplest statistical process is a lag-one auto-regressive process AR(1):

$$x_n = \rho x_{n-1} + w_n \quad (2)$$

where the current value  $x_n$  depends on the previous value and some random effect  $w_n$ , where  $\rho$  is the lag-one autocorrelation coefficient ( $0 \leq \rho \leq 1$ ) [3]. The AR(1) process is characterized by an exponentially decaying Autocorrelation Function (ACF) and when the Partial Autocorrelation Function (PACF) exhibits a single spike at the first lag. To remove the primary diurnal cycles, the raw time series in Figure 2(a) was transformed as  $x'_n = x_n - x_{n-24}$ . Figure 3 shows the ACF and PACF on the residual data.

The ACF does show a gradual decay with higher lag and the PACF has a single dominant peak at  $\text{lag} = 1$ . This largely aligns with the AR(1) process which will be assumed herein for this analysis. It should also be noted that the AR(1) process is a common null hypothesis for stochastic variability in climate system. However, a few secondary PACF spikes are apparent which may indicate a higher order process such as AR(2) or bending power law [10]. The AR(1) model is a robust first-order approximation that will capture most of the variance in the temperature response. It should also be noted that a similar behavior was observed for other locations than  $\mathcal{S}$  and at different years.

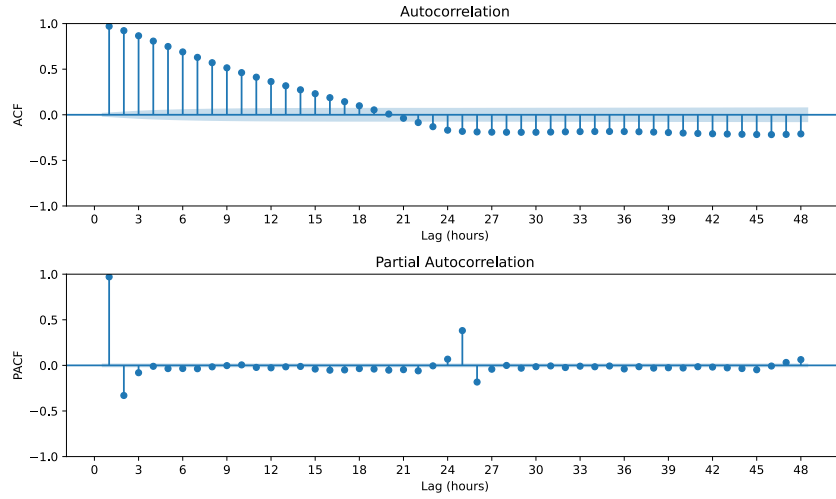


Figure 3: ACF and PACF for the sample location  $\mathcal{S}$

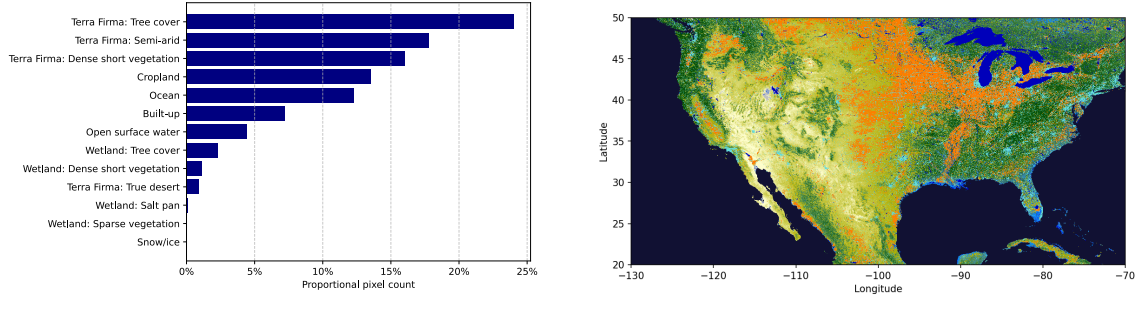
### Land Cover Data

Land cover data was obtained from the Global Land Analysis and Discovery (GLAD) laboratory [7] for the corresponding five years. The data included detailed classification from *General classes* to specific *Sub-classes*, which are more fine-grained classifications (such as bins for percent-vegetation cover or binned tree height etc.). The classification was done with decision trees [7], which introduces some uncertainty to the results herein.

Figure 4(a) shows the distribution of General classes in 2020, where Terra Firma, Croplands and Built-up being the most common classes. Figure 4(b) shows the spatial distribution of the classes, colored by predefined sub-class colors. As a brief description of the color encodings; yellow regions are vegetation, dark-green are trees, orange indicate croplands and light blue are built-up (urban regions). More detailed information about the classes can be found in the [legend](#) associated with the data.

This spatial heterogeneity is important to study along with changes in temperature trends. Surface levels can influence the memory of temperatures, since land cover types will determine how energy is stored and released from the surface, which is controlled by thermal inertia. For example, in urban environments buildings and concrete tend to absorb large amounts of heat during the day and slowly release this during the night. Therefore, the land cover will directly influence the temporal autocorrelation over time.

Since the land cover is on a much finer grid, it was down-sampled by aggregating classes to proportions on for the courser temperature grid: For every temperature grid-cell ( $0.25^\circ \times$



(a) General class distribution

(b) Land cover classification in 2020

Figure 4: Raw data and PSD for the location  $\mathcal{S}$ 

$0.25^\circ$ ), the ratio of each of the land cover classes was computed. For the analysis herein, 8 variables were derived from the GLAD dataset shown in Table 2, where each of the derived variables are fractions (0-1) for each of the temperature grid-cells.

Table 2: Derived land cover fractions from the GLAD dataset

Derived variable	Logic from GLAD classes
fraction_forest	Sub-class contains “tree”
fraction_veg_cover	Vegetation sub-class percentage (e.g., “60%”)
fraction_wetland	General Class “wetland”
fraction_desert	General class “true desert”
fraction_urban	General class “Built-up”
fraction_water	General class “open surface water”
fraction_semi_arid	General class contains “semi-arid”
fraction_cropland	General class “cropland”

Figure 5 shows the derived variables spatially over the study region in 2020. These variables will be used to analyze their effect on temporal autocorrelation.

## Modeling and Analysis

### Spectral Processing

As described in previous section, the stochastic component must be isolated in the power-spectrum (see Figure 2) in order to accurately estimate the temporal autocorrelation (the spectral exponent  $\beta$ ). A common approach in the literature is to model the stochastic component as AR(1) process and compare confidence intervals to the time-series to identify

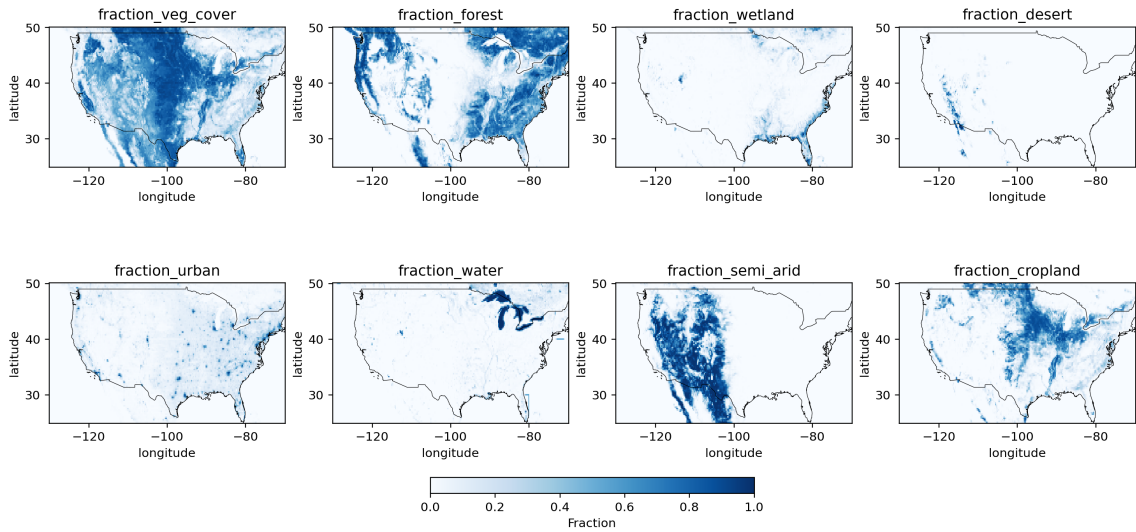


Figure 5: Derived land cover variables (2020) used in this study

harmonics (see e.g., [5]). This procedure did not work well for the temperature data, since the AR(1) model has two parameters, the variance  $\sigma^2$  and lag-1 autocorrelation coefficient  $\rho_1$ , estimated from the time-series that does often not fit the power-frequency spectrum well. This results in inaccurate identification of outliers and can bias the results. Figure A.1 shows the fitted AR(1) model to the location  $\mathcal{S}$  as an example, but the AR(1) fit varied extensively among data points.

Instead, we adopted a non-parametric approach to estimate the background stochastic noise with Locally Weighted Scatterplot Smoothing (Lowess). This method avoids a functional form as AR(1) does and is more flexible to the data, and can be tuned with the smoothing parameter  $\lambda$  (higher lambda allows for greater smoothness). The Lowess-processing method involved three main steps outlined below. The reason for a the high confidence interval of  $100 \cdot (1 - 10^{-9})\%$  was chosen to capture only clear outliers, this worked well for the data.

#### Lowess-processing:

1. **Peak detection:** A Lowess( $\lambda = 0.3$ ) curve was fitted to the PSD, and a corresponding 99.999 999 9% CI line was estimated based on a  $\chi^2_{2K}$  distribution where  $K = 3$  is the number of tapers. Powers exceeding this confidence interval were flagged as outliers.
2. **Outlier distillation:** The detected outliers were distilled by replacing the power with the average power of neighboring non-outlier points (5 on each side). This effectively smoothed out the detected outliers.

**3. Spectral leakage removal:** As described above, the MTM introduces (un-avoided) “spectral leakage” because of the finite time-series and causes harmonic power to leak into nearby frequencies, creating a localized power-hump. This was addressed by fitting two Lowess curves to the data with parameters  $\lambda = 0.8$  (stiff) and  $\lambda = 0.05$  (smooth),  $L^{stiff}$  and  $L^{smooth}$ . The smooth Lowess fit captured the localized humps while otherwise staying below the stiff Lowess fit. A positive difference (ReLU) shift was applied to the distilled-PSD powers  $P$  as:

$$P' = P - \max(0, L^{smooth} - L^{stiff}) \quad (3)$$

effectively removing the spectral leakage from the PSD.

Figure 6 shows the Lowess-processing for the sample point  $\mathcal{S}$ , effectively removing harmonic outliers and reducing spectral leakage apparent in the original PSD.

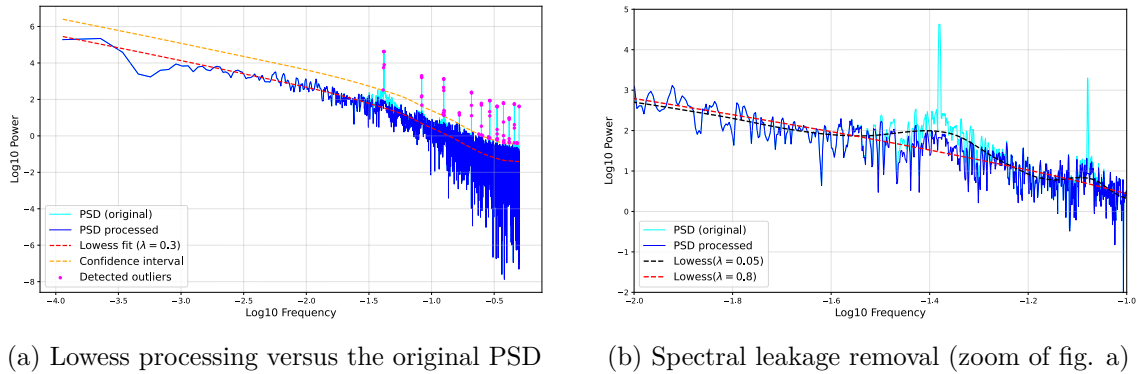


Figure 6: Lowess processing of the PSD for the location  $\mathcal{S}$

## Spectral Slope Estimation

Following the removal of harmonic powers and spectral leakage as outlined above, the temporal autocorrelation can be quantified as the (negative) fitted slope  $\beta$  based on Equation (1). Several methods have been proposed in the literature on how to estimate the spectral slope. One study [4] simply used an OLS with equally spaced log-interval means, which violates both the normality and independence assumption of OLS. Di Matteo et al. (2021) argued against this method which is statistically inaccurate, and suggested a use of bending power law (a maximum likelihood estimation) [3]. Another study used a single line fitted with GLM to account for heteroscedasticity and the non-independence of residuals [2].

The relationship between the log-power and log-frequency in Figure 6(a) does not appear to be linear, and a two linear fits (separated with a breakpoint) seems to be a more plausible

model. To deal with the heteroscedasticity, the log-frequencies were binned into 100 equally spaced log-bins (the number of bins was not found to affect the results). A piecewise OLS model did not satisfy the independence assumption and the normality assumption failed drastically, as expected. Therefore, a piecewise generalized least squares model with autoregressive errors (GLSAR) was fitted to the data.

The GLSAR model accounts for the autocorrelation of the residuals, as e.g. autoregressive process. The piecewise linear regression between the spectral power  $P(f)$  and frequency  $f$ , in log-log space, can be written as

$$\log_{10} P(f_i) = \gamma_0 + \gamma_1 \log_{10} f_i + \gamma_\Delta \max(0, \log_{10} f_i - \log_{10} f_{bp}) + \epsilon_i \quad (4)$$

where  $f_{bp}$  is the breakpoint frequency (separating the two line segments),  $\gamma_0$  is the intercept,  $\gamma_1$  is the spectral slope for the low-frequency regime ( $f < f_{bp}$ ) and  $\gamma_\Delta$  represents the change in slope for the two regimes so that

$$\gamma_2 = \gamma_1 + \gamma_\Delta$$

is the high-frequency slope. The error terms  $\epsilon_i$  are assumed to follow a lag-1 autoregressive process to account for heteroscedasticity and non-independence:

$$\epsilon_i = \rho \epsilon_{i-1} + \eta_i, \quad \eta_i \sim \mathcal{N}(0, \sigma^2) \quad (5)$$

where  $\rho$  is the lag-1 autocorrelation coefficient estimated from the residuals, and  $\eta_i$  are independent Gaussian errors. The breakpoint  $f_{bp}$  is selected by minimizing the AIC over breakpoints within the inner 80% of the frequency range.

Figure 7 shows a piecewise GLSAR fit by Eq. (4) along with a linear GLSAR fit (without any breakpoint). The piecewise linear model fits the data much better than the single slope model, which is also confirmed based on the AIC:

$$AIC_{\text{linear}} = 117.1 \quad \text{vs.} \quad AIC_{\text{piecewise}} = 4.9.$$

Both of the estimated slopes of the piecewise model ( $\gamma_1$  and  $\gamma_\Delta$ ) were significant at the significance level  $\alpha = 0.01$ , which confirms that the difference in slopes is non-zero between the two regimes. Note that the spectral exponents are  $\beta_1 = -\gamma_1$  and  $\beta_2 = -\gamma_2$ .

A Durbin-Watson (DW) statistic  $d$  is commonly used to evaluate the autocorrelation of residuals ( $0 \leq d \leq 4$ ) where  $d = 2$  indicates no autocorrelation among the residuals,  $d < 2$  suggests evidence of positive correlation and  $d > 2$  suggests negative correlation of the residuals. A “rule of thumb” is that  $d < 1$  raises an alarm for autocorrelation, implying  $\rho > 0.5$  in Eq. (5).

The significance of the DW estimates can be obtained from Durbin-Watson tables. The binned averages in Figure 7 have  $N = 81$  data points and with number of predictors  $k$ , the confidence intervals  $\mathbf{d}_L^\alpha(N, k)$  and  $\mathbf{d}_U^\alpha(N, k)$  define critical regions for hypothesis testing for a significance level  $\alpha$ . Values  $d < \mathbf{d}_L$  indicate significant positive autocorrelation,  $\mathbf{d}_L \leq d \leq \mathbf{d}_U$  is inconclusive and  $d > \mathbf{d}_U$  suggests no significant autocorrelation. For negative autocorrelation, the test statistic is compared against  $4 - \mathbf{d}_L$  and  $4 - \mathbf{d}_U$ . Table 3 summarizes the DW statistics for the piecewise and linear GLSAR models for a significance level  $\alpha = 0.01$ .

Table 3: Durbin-Watson statistics and significance levels for the fitted models

Model	$N$	$k$	$\mathbf{d}_L$	$\mathbf{d}_U$	$d$	Significant?
Piecewise GLSAR	81	2	1.440	1.541	1.005	Yes
Linear GLSAR	81	1	1.465	1.514	0.235	Yes

Note: Critical values  $d_L$  and  $d_U$  correspond to significance level ( $\alpha = 0.01$ ).

The piecewise GLSAR has a significant DW statistic of  $d = 1.005$  which suggests autocorrelation among the residuals, whilst the linear GLSAR model exhibited a significant DW statistic of  $d = 0.235$ , also implying autocorrelated errors. This indicates that additional correlation structure does remain in the data that is not fully captured by the first-order autoregressive AR(1) process. However, the piecewise model has “less“ autocorrelation among the residuals, which should be considered when interpreting the results.

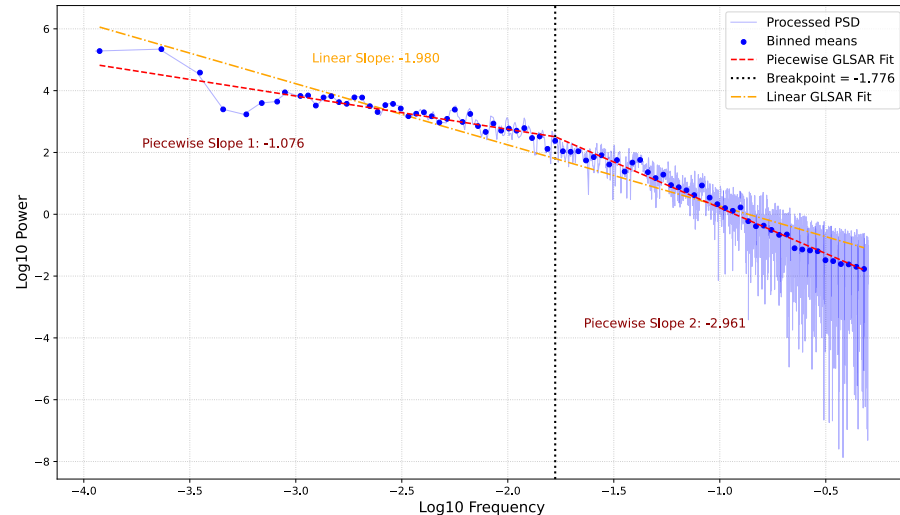


Figure 7: GLSAR fit for the sample location  $S$  (piecewise linear and linear)

These results were comparable for other instances in the data. This model fitting procedure

was applied for the entire spatial grid for each of the five years. The results for three models were captured during the execution:

- i. M1: Picewise GLSAR with a free breakpoint model by equation (4)
- ii. M2: Picewise GLSAR with daily breakpoint model by equation (4), constraining the breakpoint to the daily frequency ( $\log_{10} f^{\text{day}} \approx -1.38$ )
- iii. M3: Linear GLSAR model estimating a single slope  $\gamma_1$

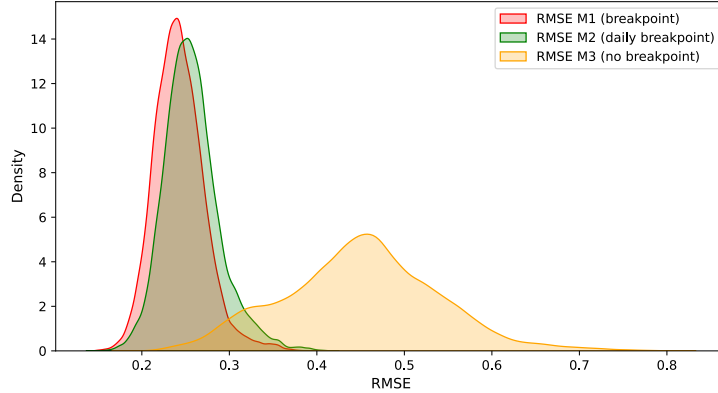


Figure 8: Density histogram of RMSE for the three models (all locations, all years)

Figure 8 shows density histogram for the RMSE of the fitted models across the region for all five years. The model with a free breakpoint (M1) exhibited the lowest RMSE values, while the distribution of the daily breakpoint model was closely comparable in distribution. The linear model without any breakpoint (M3) resulted in higher average RMSE, which was by no means not comparable to the two piecewise models.

To effectively analyze the autocorrelation (estimated as the spectral slope  $\beta$ ), the model with a fixed breakpoint (M2) will be more interpretable than model M1 and also ensuring a fair comparison of the slopes. The map of the breakpoint is shown in Appendix (Figure A.2), where lower breakpoints emerged in the *Basin and Range Province* in California, compared to the other region. This behavior needs to be investigated in future work.

The spectral slopes were estimated with a piecewise GLSAR model with a constrained breakpoint at the daily frequency (M2). Figure 9 shows the estimated spectral exponents  $\beta_1$  (low frequency regime) and  $\beta_2$  (high frequency regime) for the region (which are the negative estimated slopes in Figure 7, see Eq. (1)).

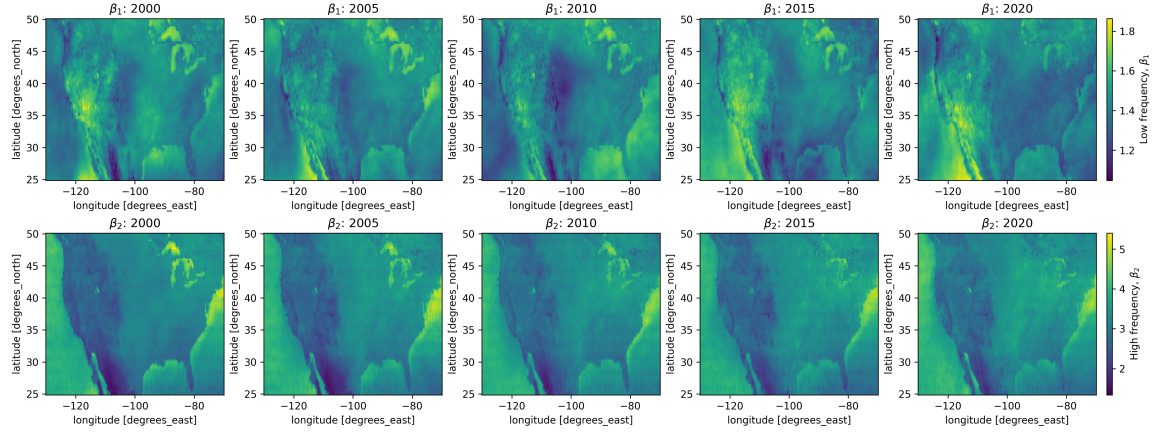


Figure 9: Estimated spectral exponents  $\beta_1$  and  $\beta_2$  for each year

### Relationship between Spectral Slopes and Land Cover

From Figure 9, there appears to be changes in the spectral exponents with time. As mentioned before, this can be affected by the land cover type, that can change over time, influencing surface properties that can affect the system's memory.

To analyze the relationship between the land cover and temporal autocorrelation (quantified with the spectral exponents  $\beta_1$  and  $\beta_2$ ), the correlation and regression slope will be investigated. The derived land cover variables (see Table 2) were used for this analysis. Figure 10 shows the relationship between the spectral exponents  $\beta_i$  and the `urban_fraction` along with the regression slope  $m$  and correlation  $\rho$ . While the standard errors are approximately normally distributed, the data points are not independent which inflates standard errors, and hence biasing corresponding p-values.

The regression slope  $m$  is strictly decreasing with time for the low-frequency spectral exponent  $\beta_1$ , indicating that the system's temperature memory is decreasing with time. Conversely, the spectral slope overall increases for the high-frequency spectral exponent  $\beta_2$ . This shows that areas observed less sub-daily memory compared to non-urban regions in the past, while in recent years they tend to stabilize high-frequency temperature fluctuations, compared to non-urban regions.

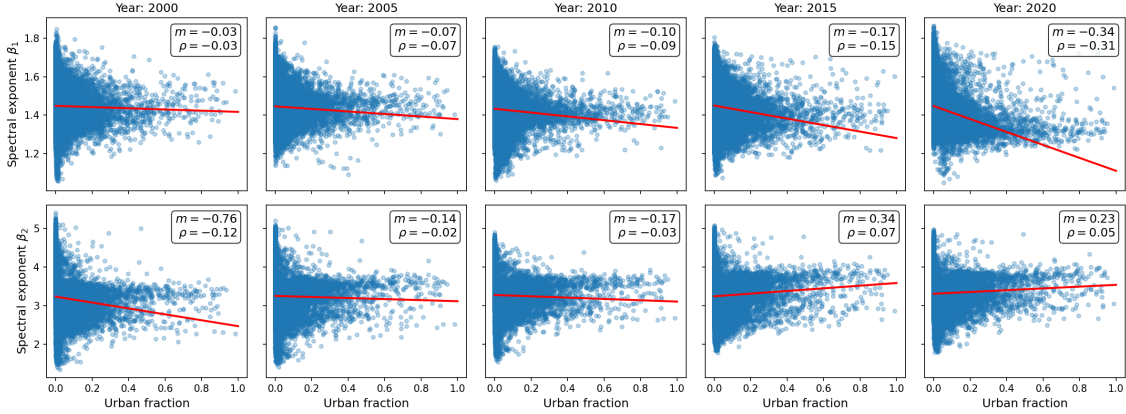


Figure 10: Spectral exponents  $\beta$  versus urban fraction, regression slope  $m$  and correlation  $\rho$

This analysis was performed for each of the derived land cover variables. Figure 11 shows the regression slope  $m$  for the spectral exponents  $\beta_1$  and  $\beta_2$  versus the land cover fractions for each of the years. Error bars indicate bootstrapped 95% confidence intervals, which were obtained through block bootstrapping with block size  $B = 10$ . The map was divided into grid-blocks of size  $B \times B$  and sampled, with replacement,  $N_{boot} = 1000$  times. Figure A.3 shows a comparable visualization for the Pearson correlation coefficient.

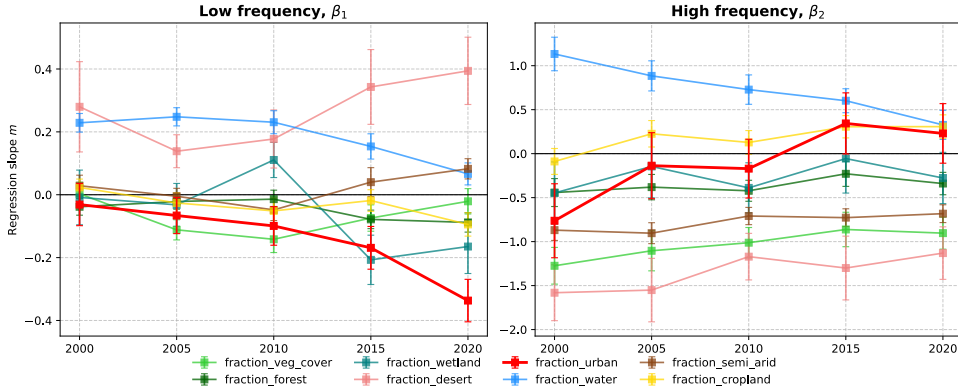


Figure 11: Regression slopes between spectral slopes  $\beta_i$  and land cover variables for every year (with 95% CI). The regression slope  $m$  between  $\beta_1$  and urban fraction strictly decreases with time.

From Figure 11, the most apparent trend is among urban fraction and  $\beta_1$ , which decreases consistently with time. In 2000, the regression slope  $m$  was not statistically significant

different from zero, while in 2020 the estimate was

$$m_{2020}^{\text{urban}} = -0.34$$

and statistically significant. The same behavior was observed for the correlation  $\rho$  in Appendix (Figure A.3). Other land cover types did not exhibit a noticeable behavior with time, except for water, which also decreases with time (with  $\gamma$  being positive). The land cover relationships are more consistent for  $\beta_2$  in Figure 11, with water fraction increasing in slope with time (while  $m$  being negative) which is intuitive since the excess heat in the system from climate change, will be absorbed by water. Additionally,  $\beta_2$  versus urban fracture increases in regression slope  $m$  over time, meaning that hourly changes exhibit less variance with time.

## Visualization and Interpretation of Results

### Spectral Memory

The spectral exponent  $\beta$  quantifies the temporal autocorrelation, which has been presented in the power-frequency domain. A more interpretable representation is to view the time-and frequency domain simultaneously. Table 4 defines three noise levels which are described by their spectral exponents  $\beta$  in the frequency domain from Equation (1) as:

$$P(f) \propto f^{-\beta} \quad \text{i.e.} \quad \log P(f) \propto -\beta \log f$$

where  $-\beta$  is the fitted slope of the  $\log P(f)$  versus  $\log f$  spectrum.

Table 4: Classification of noise colors by spectral exponent  $\beta$

Noise Color	$\beta$	Spectral memory
White noise	0	No memory (uncorrelated)
Pink noise	1	Some correlation
Red noise	2	Strong correlation

*White noise* is essentially a Gaussian noise in the time domain, corresponding to a flat line in the power-spectrum which is a memoryless system where temperature is totally independent of past values. As  $\beta$  increases, the system exhibits increasing memory. *Pink noise* ( $\beta = 1$ ) displays moderate temporal autocorrelation, while *red noise* ( $\beta = 2$ ) exhibits even stronger temporal dependence.

Figure 12 shows an illustration of how pink- and red noise translate from the time-domain to the log-log power spectral density. The red-noise time series exhibits much higher memory

(see the time domain) where the next time-steps are more dependent on the past, compared to pink-noise that is less influenced on past values. Hence, the higher value of  $\beta$  translates as a prolonged duration of temperature anomalies, such as heat waves or cold periods. A lower  $\beta$  suggests a more rapidly fluctuating system with less dependence on the past, but also less potential to store and release energy.

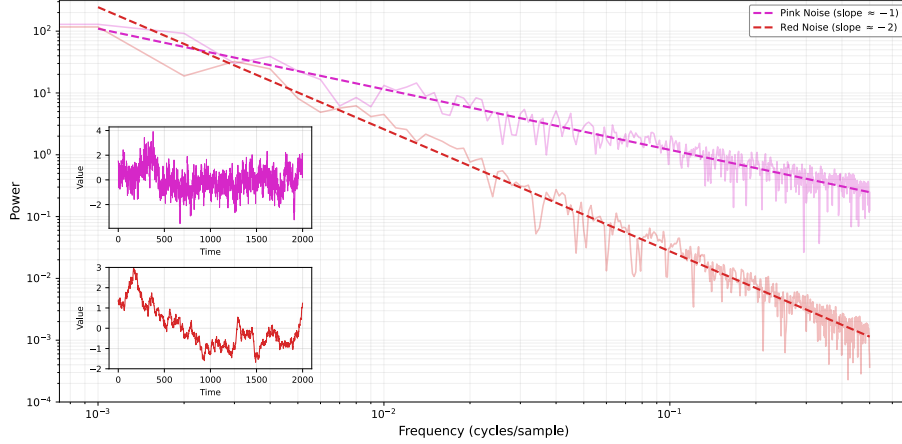


Figure 12: Relationship between time-domain and frequency-domain in terms of spectral exponent  $\beta$  (see Table 4)

### Change in Spectral Exponents

Figure 13 shows the change in the spectral exponents  $\beta_1$  and  $\beta_2$  (temporal autocorrelation) over the 20 year study period from 2000 until 2020, with physiographic divisions of the US as a reference. The observed difference indicates fundamental changes in how the variance of the surface temperature is distributed across different time scales, affecting the memory of the climate system.

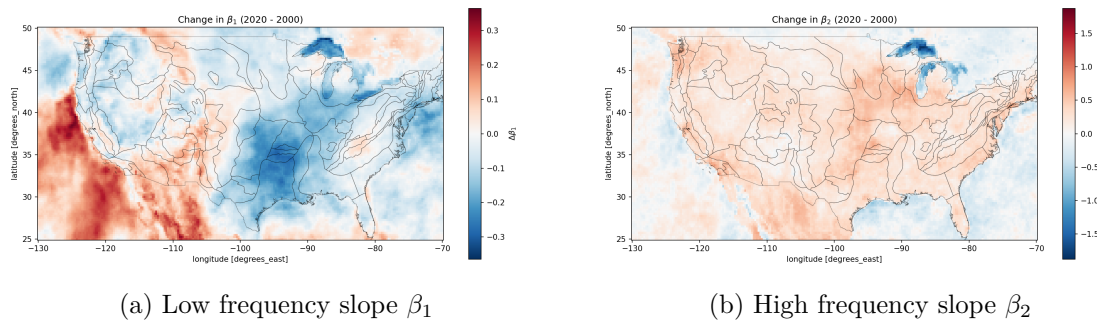


Figure 13: Difference in  $\beta_1$  and  $\beta_2$  from 2000 until 2020

Figure 13a shows that the low-frequency difference  $\Delta\beta_1$  reveals distinct patterns for marine and in-land areas. The North Pacific Ocean off the West Coast exhibits a positive change, implying that the  $\beta_1$  increases, the spectral slope becomes steeper and hence the system has an increased memory over time. This suggests that for low-frequency (longer period than one day), sea surface temperatures have become more persistent, potentially caused by ocean warming in the past decades [1]. The autocorrelation has also been found to be less on ocean areas compared to land [8], but this suggest that the temporal autocorrelation increases in the North Pacific Ocean.

On the other hand, the Interior Highlands (and nearby areas) exhibit a decrease in  $\beta_1$  over the 20 years. The low-frequency spectral slope becomes flatter over time, indicating a redistribution of variance towards higher frequencies and a corresponding decrease in the memory of the system at time scales longer than one day. This shift means that temperature fluctuations at these longer timescales have become less persistent and the system responds more quickly to perturbations in temperatures, with reduced correlation on its recent past. While urbanization was found to have most negative correlation with  $\beta_1$  (among the land covers), it is unlikely to be the primary driver of this increase due to its sparsity (see Figure 5). Changes in other land cover types or other environmental variables such as vapor pressure deficit could be contributing to the observed increase in  $\beta_1$ .

Figure 13b shows the change in high-frequency variability at the day scale and shorter. The dominant increase in  $\beta_2$  across the United States indicates a steepening of the high-frequency spectral slope. This suggests a redistribution of variance at sub-daily frequencies, where the high-frequency power (i.e. hourly) is moved towards lower-frequencies in the high-frequency regime. This means that the hourly variance has decreased and more variance is associated with daily cycles. The hourly changes have become more stable and the system has acquired more memory over short time intervals. This enhanced daily scale persistence could contribute to increased duration of extreme events such as heat waves or cold spells, which are now more likely to be sustained rather than passing by quickly.

However, the high frequency exponent  $\beta_2$  does not exhibit as apparent increase over the regions that experience the North American monsoon in the southwestern US. This can be affected by atmospheric dynamics of the monsoon which affects variance redistribution at the sub-daily scale. The Great Lakes also exhibit a different behavior, with increasing values of  $\beta_2$ , much higher than the oceans. This is interpreted as increased variability at the hourly level over time.

## Conclusions

Here we have investigated changes in temporal autocorrelation of surface air temperature across the United States in 2000-2020. Our proposed Lowess-processing effectively isolated

the stochastic component from periodic fluctuations. We utilized piecewise GLSAR models to estimate the spectral exponents  $\beta_1$  and  $\beta_2$ , which quantify the temporal autocorrelation for low- and high-frequency regimes, respectively. The results revealed that low-frequency temporal autocorrelation (with timescales longer than 24 hours) has decreased across major regions such as Pacific Northwest, New England and around Interior Highlands, indicating a reduced persistence of multi-day temperature patterns. On the other hand, high-frequency temporal autocorrelation (sub-daily scale) has increased across most of the continental US, with variance shifting from hourly fluctuations towards the daily scale. This stronger daily temperature persistence suggests that extreme temperatures are more likely to be sustained which can cause longer lasting heat waves and cold spells. This can have significant consequences on life and affect the stability of our ecosystem.

The comparison with the GLAD land cover dataset revealed an decreasing relationship between urbanization and low-frequency temporal autocorrelation with time, which was insignificant in 2000 but  $\gamma = -0.34$  in 2020 and significant. This means that urban regions have less low-frequency memory than they used to have. These results also show that land cover change can influence temperature persistence to some extent.

For future work, this analysis can be directly extended to analyze longer time periods than discrete years as herein. This would introduce annual frequencies and longer-period oscillations which might reveal different patterns than we have observed. Additionally, higher order auto-regressive models should be explored to mitigate the residual autocorrelation as we found with the AR(1) errors, which could yield a more accurate estimates of the spectral slopes. Furthermore, the identified persistence of hourly temperatures should be quantified explicitly by comparing the duration of heat waves and cold spells in recent years to the past. This would confirm hour hypothesis that high-frequency (hourly) variance has decreased overall in the continental United States in the past 20 years.

## References

- [1] Lijing Cheng, Karina von Schuckmann, John P Abraham, Kevin E Trenberth, Michael E Mann, Laure Zanna, Matthew H England, Jan D Zika, John T Fasullo, Yongqiang Yu, et al. Past and future ocean warming. *Nature Reviews Earth & Environment*, 3(11):776–794, 2022.
- [2] Grace J Di Cecco and Tarik C Gouhier. Increased spatial and temporal autocorrelation of temperature under climate change. *Scientific reports*, 8(1):14850, 2018.
- [3] S Di Matteo, Nicholeen M Viall, and L Kepko. Power spectral density background estimate and signal detection via the multitaper method. *Journal of Geophysical Research: Space Physics*, 126(2):e2020JA028748, 2021.
- [4] Peter Huybers and William Curry. Links between annual, milankovitch and continuum temperature variability. *Nature*, 441(7091):329–332, 2006.
- [5] Michael E Mann and Jonathan M Lees. Robust estimation of background noise and signal detection in climatic time series. *Climatic change*, 33(3):409–445, 1996.
- [6] Donald B Percival and Andrew T Walden. *Spectral analysis for physical applications*. cambridge university press, 1993.
- [7] Peter Potapov, Matthew C Hansen, Amy Pickens, Andres Hernandez-Serna, Alexandra Tyukavina, Svetlana Turubanova, Viviana Zalles, Xinyuan Li, Ahmad Khan, Fred Stolle, et al. The global 2000-2020 land cover and land use change dataset derived from the landsat archive: first results. *Frontiers in Remote Sensing*, 3:856903, 2022.
- [8] John H Steele. A comparison of terrestrial and marine ecological systems. *Nature*, 313(6001):355–358, 1985.
- [9] David A Vasseur, John P DeLong, Benjamin Gilbert, Hamish S Greig, Christopher DG Harley, Kevin S McCann, Van Savage, Tyler D Tunney, and Mary I O’Connor. Increased temperature variation poses a greater risk to species than climate warming. *Proceedings of the royal society B: biological sciences*, 281(1779):20132612, 2014.
- [10] S Vaughan, RJ Bailey, and DG Smith. Detecting cycles in stratigraphic data: Spectral analysis in the presence of red noise. *Paleoceanography*, 26(4), 2011.

## Appendix

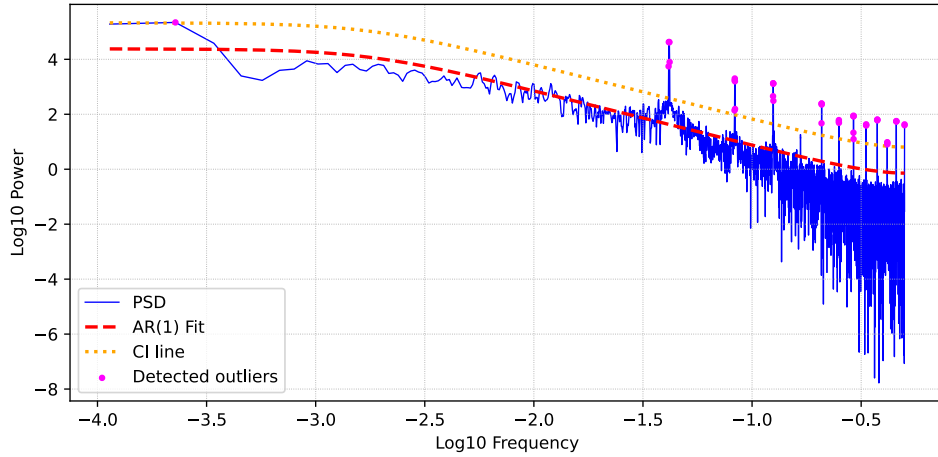


Figure A.1: Outlier detection using AR(1) model for the location  $\mathcal{S}$  (99.999 999 9% CI)

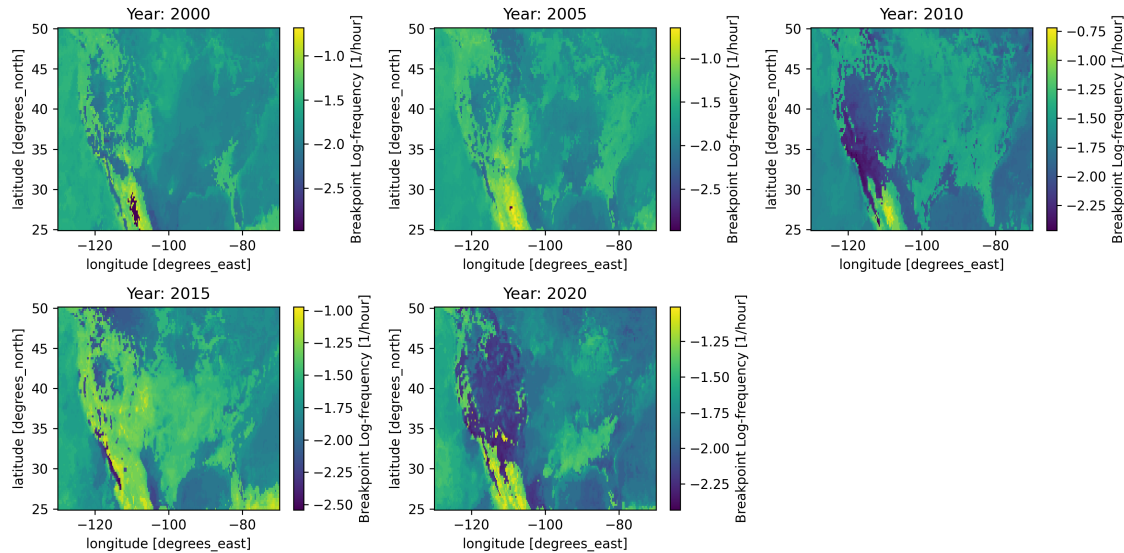


Figure A.2: Estimated breakpoints for model M1 for each year

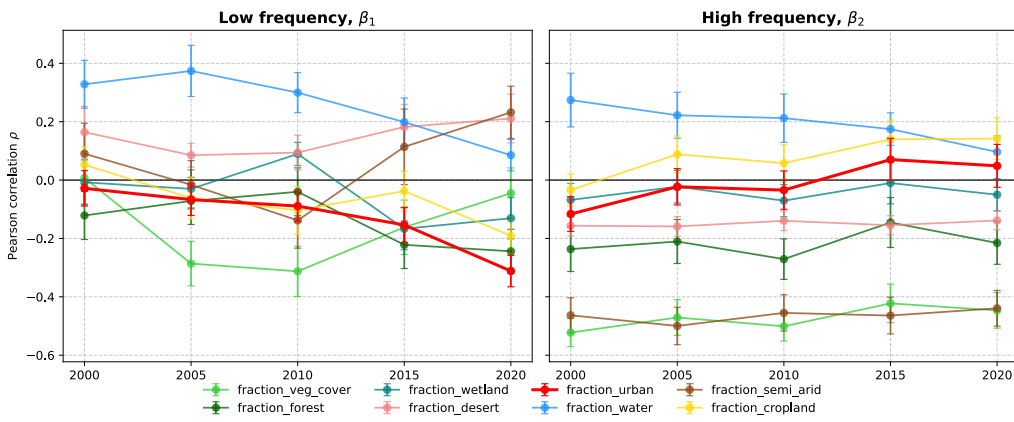


Figure A.3: Correlation between spectral slopes  $\beta$  and land cover variables for every year